

Regina Schmitt · Ralf Müller · Charlotte Kuhn ·
Herbert M. Urbassek

A phase field approach for multivariant martensitic transformations of stable and metastable phases

Received: 5 June 2012 / Accepted: 7 December 2012 / Published online: 11 January 2013
© Springer-Verlag 2013

Abstract A phase field model approach for multivariant martensitic transformations of stable and metastable phases is introduced. The evolution of the microstructure is examined with respect to elastic energy minimization in which one or two martensitic orientation variants are considered. In this context, the martensitic nucleation behavior is simulated for different activation barriers. Furthermore, the influence of time-dependent external loads on the formation of the different phases is studied. The numerical implementation is performed with finite elements and an implicit time integration scheme.

Keywords Phase field model · Phase transformation · Finite elements ·

1 Introduction

Due to its mechanical properties, the martensitic phase is often desirable. In the last decade, atomistic simulation contributed to an understanding of the dynamics of martensitic transformations. These simulations started with an investigation of the NiAl system [14]. But soon attention turned to ferrous alloys, where at first martensitic transformations in the $\text{Fe}_{1-x}\text{Ni}_x$ system were simulated [6]. These investigations were later also extended to pure Fe, where both strain- and temperature-induced transformations could be analyzed [5]. As a drawback, length scales beyond ~ 100 nm and time scales beyond a few nanoseconds are only difficult to access in atomistic simulations. However, atomistic transformations offer the advantage that details on the transformation pathway (such as the atomic relocations) become accessible [15]. In addition, the energetics of the transition are naturally included in the interatomic interaction forces.

On a larger length scale, the continuum mechanical aspects of phase transformations in solids are given in [7]. Bartel et al. [2] propose a micromechanical model for martensitic transformations using the concept of energy relaxation, where laminates are introduced in order to determine a quasiconvex energy hull.

In another approach, sharp interfaces between the phase boundaries are assumed. In [4], the concept of moving boundaries is applied to model the martensitic transformation. However, the numerical realization of this approach is generally difficult. Alternatively, the evolution of microstructure can be described using a phase field model which is in mathematical terms the regularization of a sharp interface approach. Within this approach, the different phases are represented by a scalar valued order parameter which allows a diffuse transition zone between the phases. Based on [3] and [19], several micro-elastic phase field models for martensitic transformations have been developed, for example, [11]. There are models which additionally consider

R. Schmitt (✉) · R. Müller · C. Kuhn
Institute of Applied Mechanics, University of Kaiserslautern, Gottlieb-Daimler-Straße, 67663 Kaiserslautern, Germany
E-mail: rschmitt@rhrk.uni-kl.de

H. M. Urbassek
Physics Department and Research Center OPTIMAS, University of Kaiserslautern, Erwin-Schrödinger-Straße,
67663 Kaiserslautern, Germany

plasticity [21] and dislocation kinetics [12]. In [1] Artemev et al. examine martensitic transformations under external load. All of these phase field models are based on fast Fourier transformation while Yamanaka [21] applies the finite difference method to solve the field equations. However, for considering complicated boundary conditions or complex material laws, the finite element method is more effective. It is used, for example, by Levitas et al. in [13] and Hildebrand and Miehe in [9] for a martensitic phase field model. Hildebrand and Miehe model two stable phases. The interface motion is induced through Dirichlet boundary conditions. In a more recent work [10]; Hildebrand and Miehe model two-variant martensitic laminates at large strains. In this work, the two stable states of the double well function correspond to two different martensitic orientation variants. In [13], a thermomechanical model is proposed which considers the crystallographically induced eigenstrain. The double well functions are chosen in a way that stable and metastable phases could be defined. However, Levitas et al. in [13] use the same elastic compliance tensor for both phases so that the different elastic properties of the phases cannot be taken into account.

In the present work, we apply a finite element scheme. The double well function considers stable and metastable phases such that the modeling of more than one martensitic orientation variant is possible. The influence of the temperature on the microstructural evolution can be modeled by a proper choice of the parameters of the separation potential. Additionally, we regard the different elastic properties of each phase since the elasticity tensor depends linearly on the order parameter. Furthermore, the transformation-induced eigenstrain which leads to interface motion without applying external loads is significant for the model. However, we focus on the deformation-induced α' -martensite, which is generated by applying defined mechanical loads on the metastable austenitic phase. With the aid of the phase field model, the impact of a mechanical load history on the formation of different α' -martensitic orientation variants with different transformation-induced eigenstrains ϵ_i^0 is studied in detail. In this context, the energy evolution during nucleation and growth of the martensitic phases is also considered.

2 A phase field approach for multivariant martensitic transformations

In the phase field model, an order parameter c_i indicates the present phase: $c_i = 0$ in the austenitic phase and $c_i = 1$ in the i th martensitic orientation variant. In this work, we consider up to two variants. The phase field approach is based upon the minimization of the global free energy $F = \int_V \psi \, dV$. The energy density or phase field potential ψ is additively split into three parts: the elastic energy W , the phase separation potential ψ^{sep} and the gradient energy ψ^{grad} [16]:

$$\psi(\epsilon, c_i, \nabla c_i) = W(\epsilon, c_i) + \psi^{\text{sep}}(c_i) + \psi^{\text{grad}}(\nabla c_i), \quad (1)$$

where

$$\psi^{\text{sep}}(c_i) = \kappa_s \frac{G}{L} f(c_i) \quad \text{and} \quad (2)$$

$$\psi^{\text{grad}}(\nabla c_i) = \frac{1}{2} \kappa_g G L \sum_{i=1}^2 \|\nabla c_i\|^2. \quad (3)$$

For properly chosen calibration constants κ_s and κ_g , the parameter G appearing in both terms can be identified as the characteristic interface energy density while L controls the width of the transition zone between the phases [18]. The phase separation potential can be formulated using the Landau polynomial expansion [21]

$$f(c_i) = 1 + \frac{A}{2} (c_1^2 + c_2^2) - \frac{B}{3} (c_1^3 + c_2^3) + \frac{C}{4} (c_1^2 + c_2^2)^2. \quad (4)$$

In the plot of $f(c_i)$ in Fig. 1a, it can be seen that the function has a local minimum of value 1 at $(0, 0)$ which corresponds to the metastable austenitic phase and an absolute minimum of value 0 at $(1, 0)$ and at $(0, 1)$ corresponding to the stable martensitic orientation variants 1 and 2, respectively. As for these stable states holds $f = 0$, there is no energy contribution by means of ψ^{sep} . The dimensionless coefficients A , B and C define the shape of $f(c_i)$. For this work (excluding Sect. 4.2), $A = 0.15$, $B = 3A + 12$ and $C = 2A + 12$ were chosen as in [21]. For the transformation from the austenitic phase to the martensitic phase, that is, for the change of $c_i = 0$ to $c_i = 1$, the system has to overcome an energy barrier Δf which is indicated in Fig. 1b, where f is plotted for a single orientation variant. The value of Δf depends on the choice of the parameters A , B and C .

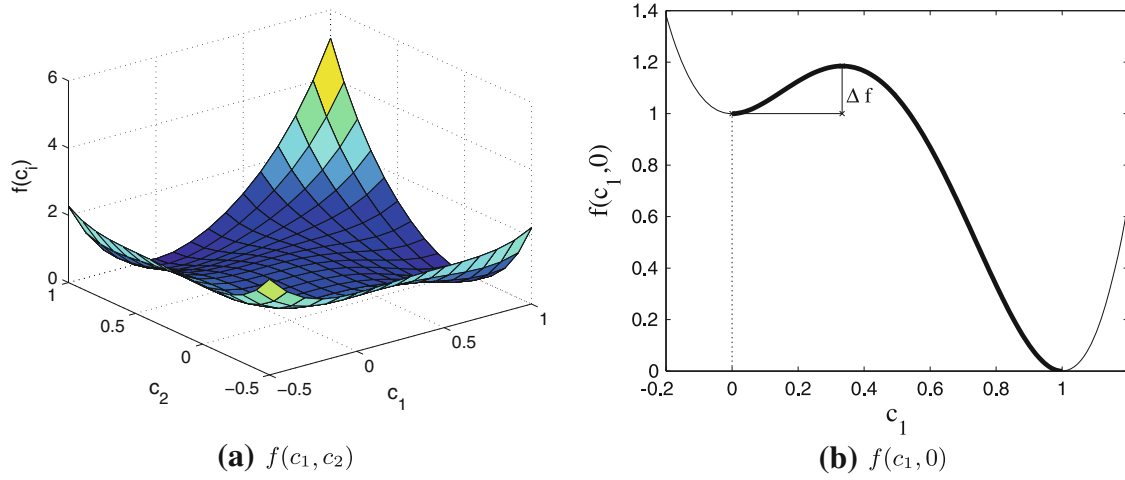


Fig. 1 Landau polynomial expansion $f(c_i) = f(c_1, c_2)$

Furthermore, the **elastic energy** in (1) is defined as

$$W(\boldsymbol{\varepsilon}, c_i) = \frac{1}{2} [\boldsymbol{\varepsilon} - \boldsymbol{\varepsilon}^0(c_i)] : \mathbb{C}(c_i) [\boldsymbol{\varepsilon} - \boldsymbol{\varepsilon}^0(c_i)], \quad (5)$$

where the **material tensor** $\mathbb{C}(c_i)$ denotes the elastic stiffness

$$\mathbb{C}(c_i) = \mathbb{C}_A + c_1 (\mathbb{C}_M - \mathbb{C}_A) + c_2 (\mathbb{C}_M - \mathbb{C}_A). \quad (6)$$

The indices A and M refer to the austenitic and martensitic phase, respectively. It is **assumed that the elastic stiffness of the two martensite variants is identical**. This assumption is made as no details on the elasticity tensor of the martensite variants are available. If necessary, this information can readily be considered in the model and the numerical realization. In Eq. (5), $\boldsymbol{\varepsilon}$ denotes the linearized strain tensor related to the displacement field \mathbf{u} by

$$\boldsymbol{\varepsilon}(\mathbf{u}) = \frac{1}{2} (\nabla \mathbf{u} + (\nabla \mathbf{u})^T), \quad (7)$$

while $\boldsymbol{\varepsilon}^0(c_i)$ considers the transformation-induced eigenstrain defined as

$$\boldsymbol{\varepsilon}^0(c_i) = c_1 \boldsymbol{\varepsilon}_1^0 + c_2 \boldsymbol{\varepsilon}_2^0. \quad (8)$$

Considering the axis of the austenitic cubic phase as the reference coordinate system, $\boldsymbol{\varepsilon}_1^0$ and $\boldsymbol{\varepsilon}_2^0$ can be written in terms of the crystal lattice parameters a_A of the austenitic phase and a_M, c_M of the martensitic phase [21]. For a plane strain problem, the eigenstrains $\boldsymbol{\varepsilon}_1^0$ and $\boldsymbol{\varepsilon}_2^0$ read

$$\boldsymbol{\varepsilon}_1^0 = \begin{bmatrix} \frac{a_M - a_A}{a_A} & 0 \\ 0 & \frac{c_M - a_A}{a_A} \end{bmatrix} \quad \text{and} \quad \boldsymbol{\varepsilon}_2^0 = \begin{bmatrix} \frac{c_M - a_A}{a_A} & 0 \\ 0 & \frac{a_M - a_A}{a_A} \end{bmatrix}. \quad (9)$$

To describe the evolution of the microstructure, the **rates** \dot{c}_i are assumed to be proportional to the variational derivative of the phase field potential ψ with respect to c_i

$$\dot{c}_i = -M \frac{\delta \psi}{\delta c_i} = -M \left[\frac{\partial W}{\partial c_i} + G \left(\frac{\kappa_s}{L} \frac{\partial f}{\partial c_i} - \kappa_g L \Delta c_i \right) \right], \quad i = 1, 2 \quad (10)$$

which is known as the **time-dependent Ginzburg–Landau equation (TDGL)**. The **mobility factor** M describes the kinetics of the process. In addition to the TDGL, the **mechanical fields** have to satisfy balance laws,

Neglecting inertia effects and in the absence of volume forces, the balance of linear momentum reduces to the equilibrium condition

$$\operatorname{div} \boldsymbol{\sigma} = \mathbf{0} \quad (11)$$

for the Cauchy stress tensor $\boldsymbol{\sigma}$. The stresses are given by the constitutive relation

$$\boldsymbol{\sigma} = \frac{\partial \psi}{\partial \boldsymbol{\varepsilon}} = \mathbb{C}(c_i) (\boldsymbol{\varepsilon} - \boldsymbol{\varepsilon}^0(c_i)). \quad (12)$$

Due to the dependence of \mathbb{C} and $\boldsymbol{\varepsilon}^0$ on the phase field variables c_i , Eqs. (10) and (11) represent a coupled nonlinear time-dependent problem, which is solved by a finite element scheme.

3 Numerical implementation

The phase field model was implemented into a two-dimensional finite element framework with the displacements \mathbf{u} and the order parameters c_1 and c_2 as nodal degrees of freedom. The weak forms of Eqs. (11) and (10) read for $i = 1, 2$ with the test functions $\boldsymbol{\eta}_u, \eta_{c_i}$

$$\int_V \nabla \boldsymbol{\eta}_u : \boldsymbol{\sigma} \, dV = \int_{\partial V_i} \boldsymbol{\eta}_u \mathbf{t}^* \, dA. \quad (13)$$

and

$$\int_V \eta_{c_i} \frac{\dot{c}_i}{M} \, dV - \int_V \nabla \eta_{c_i} \mathbf{q}_i \, dV + \int_V \eta_{c_i} \left(\frac{\partial W}{\partial c_i} + G \frac{\kappa_s}{L} \frac{\partial f}{\partial c_i} \right) \, dV = - \int_V \eta_{c_i} q_i^* \, dA, \quad i = 1, 2 \quad (14)$$

where $\mathbf{q}_i = -\kappa_g G L \nabla c_i$. The boundary conditions for the stresses $\boldsymbol{\sigma}$ is the traction $\mathbf{t}^* = \boldsymbol{\sigma} \mathbf{n}$ and for \mathbf{q}_i the normal flux $q_i^* = \mathbf{q}_i \cdot \mathbf{n}$ with $q_i^* = 0$, where \mathbf{n} is the outer normal vector to the volume V .

Using Voigt notation, which is denoted by an underbar $\underline{(\cdot)}$, for the 2d-plane strain problem, the discretization of \mathbf{u} , $\boldsymbol{\varepsilon}$ and $c_i, \nabla c_i$ with shape functions N_I for node I is

$$\underline{\mathbf{u}} = \sum_{I=1}^N N_I \hat{\underline{\mathbf{u}}}_I, \quad \underline{\boldsymbol{\varepsilon}} = \sum_{I=1}^N \underline{\mathbf{B}}_I^u \hat{\underline{\mathbf{u}}}_I, \quad (15)$$

$$c_i = \sum_{I=1}^N N_I \hat{c}_{iI}, \quad \underline{\nabla c_i} = \sum_{I=1}^N \underline{\mathbf{B}}_I^{c_i} \hat{c}_{iI}, \quad i = 1, 2 \quad (16)$$

$$\dot{c}_i = \sum_{I=1}^N N_I \hat{\dot{c}}_{iI} \quad (17)$$

where

$$\underline{\mathbf{B}}_I^u = \begin{bmatrix} N_{I,x} & 0 \\ 0 & N_{I,y} \\ N_{I,y} & N_{I,x} \end{bmatrix} \quad \text{and} \quad \underline{\mathbf{B}}_I^{c_i} = \begin{bmatrix} N_{I,x} \\ N_{I,y} \end{bmatrix}. \quad (18)$$

The nodal quantities are denoted by the superimposed hat $\hat{(\cdot)}$. With these discretizations applied to the left hand sides of Eqs. (13) and (14), one obtains the nodal residuals as a function of the nodal degrees of freedom $\hat{\underline{\mathbf{d}}}_J = (\hat{\underline{\mathbf{u}}}_J, c_{1J}, c_{2J})^T$ and the rates $\hat{\underline{\mathbf{d}}}_J$,

$$\underline{\mathbf{R}}_I(\hat{\underline{\mathbf{d}}}_J, \hat{\dot{\underline{\mathbf{d}}}}_J) = \begin{bmatrix} \underline{\mathbf{R}}_I^u(\hat{\underline{\mathbf{d}}}_J, \hat{\dot{\underline{\mathbf{d}}}}_J) \\ \underline{\mathbf{R}}_I^{c_1}(\hat{\underline{\mathbf{d}}}_J, \hat{\dot{\underline{\mathbf{d}}}}_J) \\ \underline{\mathbf{R}}_I^{c_2}(\hat{\underline{\mathbf{d}}}_J, \hat{\dot{\underline{\mathbf{d}}}}_J) \end{bmatrix} = \begin{bmatrix} \int_V (\underline{\mathbf{B}}_I^u)^T \underline{\boldsymbol{\sigma}} \, dV \\ \int_V N_I \frac{\dot{c}_1}{M} \, dV - \int_V \underline{\mathbf{B}}_I^{c_1 T} \mathbf{q}_1 \, dV + \int_V N_I \left(\frac{\partial W}{\partial c_1} + G \frac{\kappa_s}{L} \frac{\partial f}{\partial c_1} \right) \, dV \\ \int_V N_I \frac{\dot{c}_2}{M} \, dV - \int_V \underline{\mathbf{B}}_I^{c_2 T} \mathbf{q}_2 \, dV + \int_V N_I \left(\frac{\partial W}{\partial c_2} + G \frac{\kappa_s}{L} \frac{\partial f}{\partial c_2} \right) \, dV \end{bmatrix}. \quad (19)$$

The time integration of the transient terms is done with the backward Euler method. The stiffness matrix $\underline{\mathbf{K}}_{IJ}$ is given by

$$\underline{\mathbf{K}}_{IJ} = \frac{\partial \underline{\mathbf{R}}_I}{\partial \hat{\underline{\mathbf{d}}}_J} = \begin{bmatrix} \underline{\mathbf{K}}_{IJ}^{uu} & \underline{\mathbf{K}}_{IJ}^{uc1} & \underline{\mathbf{K}}_{IJ}^{uc2} \\ \underline{\mathbf{K}}_{IJ}^{c1u} & \underline{\mathbf{K}}_{IJ}^{c1c1} & \underline{\mathbf{K}}_{IJ}^{c1c2} \\ \underline{\mathbf{K}}_{IJ}^{c2u} & \underline{\mathbf{K}}_{IJ}^{c2c1} & \underline{\mathbf{K}}_{IJ}^{c2c2} \end{bmatrix}, \quad (20)$$

where the matrix entries can be calculated with $\tilde{\underline{\boldsymbol{\sigma}}} = (\underline{\mathbb{C}}_M - \underline{\mathbb{C}}_A) (\underline{\boldsymbol{\varepsilon}} - \underline{\boldsymbol{\varepsilon}}^0(c_i))$ and $\underline{\boldsymbol{\sigma}}_i^0 = \underline{\mathbb{C}}(c_i) \underline{\boldsymbol{\varepsilon}}_i^0$ as follows (for $i, j = 1, 2$):

$$\begin{aligned} \underline{\mathbf{K}}_{IJ}^{uu} &= \int_V (\underline{\mathbf{B}}_I^u)^T \underline{\mathbb{C}} \underline{\mathbf{B}}_J^u dV \\ \underline{\mathbf{K}}_{IJ}^{uc_i} &= \underline{\mathbf{K}}_{IJ}^{c_i u} = \int_V (\underline{\mathbf{B}}_I^u)^T (\tilde{\underline{\boldsymbol{\sigma}}} - \underline{\boldsymbol{\sigma}}_i^0) N_J dV \\ \underline{\mathbf{K}}_{IJ}^{c_i c_i} &= \int_V \kappa_g GL (\underline{\mathbf{B}}_I^{c_i})^T \underline{\mathbf{B}}_J^{c_i} + N_I \left((\underline{\boldsymbol{\varepsilon}}_i^0)^T (\underline{\boldsymbol{\sigma}}_i^0 - 2\tilde{\underline{\boldsymbol{\sigma}}}) + \kappa_s \frac{G}{L} \frac{\partial^2 f}{\partial c_i^2} \right) N_J dV \\ \underline{\mathbf{K}}_{IJ}^{c_i c_j} &= \int_V N_I \left(-\tilde{\underline{\boldsymbol{\sigma}}} (\underline{\boldsymbol{\varepsilon}}_i^0 + \underline{\boldsymbol{\varepsilon}}_j^0) + \underline{\boldsymbol{\varepsilon}}_j^0 \underline{\boldsymbol{\sigma}}_i^0 + \kappa_s \frac{G}{L} \frac{\partial^2 f}{\partial c_i \partial c_j} \right) N_J dV \quad (i \neq j). \end{aligned}$$

The damping matrix $\underline{\mathbf{D}}_{IJ}$ reads

$$\underline{\mathbf{D}}_{IJ} = \frac{\partial \underline{\mathbf{R}}_I}{\partial \hat{\underline{\mathbf{d}}}_J} = \int_V \begin{bmatrix} 0 & 0 & 0 & 0 \\ 0 & 0 & 0 & 0 \\ 0 & 0 & \frac{1}{M} N_I^2 & 0 \\ 0 & 0 & 0 & \frac{1}{M} N_I^2 \end{bmatrix} dV. \quad (21)$$

To evaluate the integrals Gauß quadrature is used.

4 Numerical simulation

The model was implemented into a four-node quadrilateral plane element with bilinear shape functions. In the following illustrative, numerical examples of the evolution of martensitic phases are presented. For all calculations, the elasticity tensors

$$\underline{\mathbb{C}}_A = \begin{bmatrix} 1.40 & 0.84 & 0.00 \\ 0.84 & 1.40 & 0.00 \\ 0.00 & 0.00 & 0.28 \end{bmatrix} 10^5 \frac{\text{N}}{\text{mm}^2}, \quad \underline{\mathbb{C}}_M = 1.1 \underline{\mathbb{C}}_A \frac{\text{N}}{\text{mm}^2} \quad (22)$$

and the eigenstrains

$$\underline{\boldsymbol{\varepsilon}}_1^0 = \begin{bmatrix} -0.1 \\ 0.1 \\ 0.0 \end{bmatrix} \quad \underline{\boldsymbol{\varepsilon}}_2^0 = \begin{bmatrix} 0.1 \\ -0.1 \\ 0.0 \end{bmatrix} \quad (23)$$

are considered in Voigt notation. The stiffness $\underline{\mathbb{C}}_A$ and the eigenstrains have been taken over from [21]. These eigenstrains describe a simple shear lattice distortion where one of the cubic axes is expanded while the other one is compressed by the same amount. The calibration constants are determined with $\kappa_s = 1.3592$ and $\kappa_g = 0.6960$ so that $G = 0.1 \frac{\text{J}}{\text{m}^2}$ is a measure for the characteristic interface energy density. This value lies within the range of the characteristic energy densities of other phase field models [17]. The length $L = 5 \text{ nm}$ is

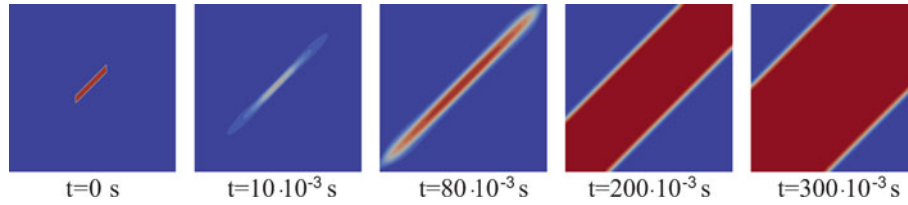


Fig. 2 Formation of the martensitic phase (single variant, *red*) for a nucleus in diagonal direction. (Color figure online)

chosen sufficiently small in comparison to the edge length of the quadratic computation domain of 176.5 nm. The considered mobility constant for the simulations is $M = 1.0 \times 10^{-6} \frac{\text{m}^3}{\text{Js}}$.

For the first calculations, only one orientation variant is considered and no external loads are applied so that the boundaries are stress free. In that way, the formation of one individual martensitic phase can be studied.

4.1 Nucleus in diagonal direction

In Fig. 2, the first picture shows the initial configuration where the austenitic matrix is depicted in blue. It contains a martensitic nucleus in diagonal direction, indicated in red. The martensitic nucleus is subjected to the eigenstrain so that the microstructure evolves even though there is no mechanical loading. For the nucleus, the order parameter is set to $c_1 = 0.9$ so that c_1 is not in the stable minimum at $c_1 = 1$. At first the nucleus shrinks as c_1 approaches 0 in order to minimize the total energy by minimization of the elastic energy W . However, for c_1 approaching 0, the separation potential ψ^{sep} increases. When the separation potential ψ^{sep} has grown to a certain amount (and the energy barrier Δf is not too high), it gets energetically favorable for the system to minimize ψ^{sep} instead of W . This means c_1 approaches the stable minimum at $c_1 = 1$ so the martensitic phase starts to grow. In the third picture of Fig. 2 for $t = 80 \times 10^{-3}$ s, it can be seen that the martensite grows in diagonal direction keeping a thin plate-like shape. When the plate has grown completely through the computation domain, the martensitic phase extends in lateral direction until the matrix is entirely martensitic. This plate-like shape of the growing martensite is confirmed by theoretical studies of the martensitic transformation [21]. Additionally, the diagonal growing direction of the plate coincides with crystallographic (geometrical) theories [20]. However, the formation of the martensitic phase in this example could have been influenced by the initial conditions as the nucleus is set in diagonal direction and already has an elongated shape.

4.2 Randomly distributed circular nuclei

In the following calculations—where still only one variant is considered and no external loads are applied—ten circular martensitic nuclei are distributed randomly in the matrix (Fig. 3, $t = 0$ s). This configuration generalizes a lattice containing randomly distributed defects which may serve as nuclei for the martensitic transformation. It corresponds to the initially randomly distributed fields in [13]. With this initial configuration, three calculations are performed for different separation potentials ψ^{sep} with varying energy barriers Δf . For the first simulation (Fig. 3a) $\Delta f_1 \approx 7.8 \times 10^{-6}$, for the second one $\Delta f_2 \approx 5.4 \times 10^{-4}$ (Fig. 3b) and $\Delta f_3 \approx 4.9 \times 10^{-3}$ for the third calculation (Fig. 3c). It can be seen that the lowest energy barrier Δf_1 is overcome fastest and the martensitic phase grows in diagonal direction in the shape of thin plates which is not preset by the initial conditions. To overcome Δf_2 , the system needs more time steps so that at $t = 50 \times 10^{-3}$ s the martensite fraction is lower than in Fig. 3a. The third energy barrier is too high so that the order parameter c_1 remains in the local minimum at $c_1 = 0$ and the martensite does not nucleate. These separation potentials ψ^{sep} with different energy barriers Δf correspond to different temperatures with varying martensite activation barriers. Thus, the nucleation behavior can be adjusted by the coefficients A , B and C in the Landau polynomial $f(c_i)$.

4.3 Nucleus in diagonal direction, 2 variants

To gain a basic understanding of the transformation behavior for two martensitic orientation variants, the example with one nucleus in diagonal direction ($c_1 = 0.9$) is calculated again without external load, however

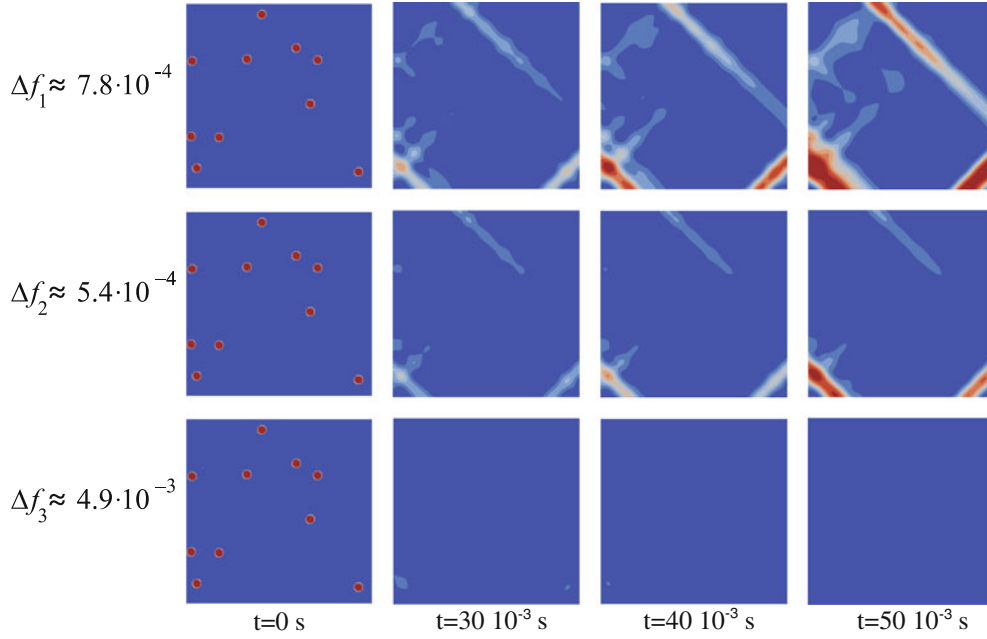


Fig. 3 Formation of the martensitic phase (single variant, *red*) for ten circular nuclei, randomly distributed. (Color figure online)

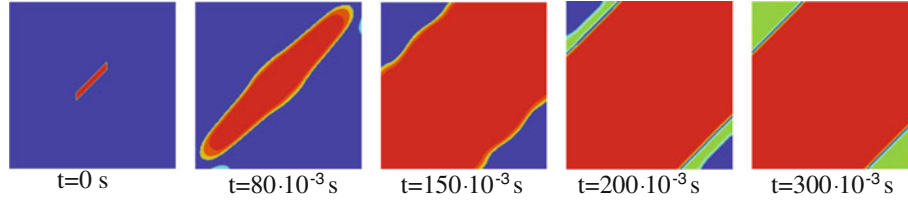


Fig. 4 Formation of the martensitic phase (variant 1: *red*, variant 2: *green*) for a nucleus (variant 1) in diagonal direction. (Color figure online)

with the second orientation variant taken into account. The evolution of the phases is plotted in Fig. 4, where the second orientation variant is depicted in green. For figures containing two orientation variants, the color scale ranges from blue (austenite) over green (second orientation variant) to red (first orientation variant). So for this color scale, the interface region around the first martensitic variant is depicted in yellow and the interface region around the second martensitic orientation variant is shown in light blue. In comparison to Fig. 2, the system with two variants nucleates significantly faster. As stated in Sect. 4.1, initially the total energy is reduced by minimization of W , so the nucleus shrinks. However, in this case due to the different signs of ϵ_1^0 and ϵ_2^0 , W is additionally minimized in that in the area of the nucleus c_1 and c_2 are approaching the same value. This means c_2 starts to grow in the nucleus region. Thus, the separation potential ψ^{sep} grows faster than for the single variant in Sect. 4.1 and eventually causes a faster nucleation. The nucleation might be twin related for a three-dimensional problem. However, in this two-dimensional case, the second variant retreats in the vicinity of the nucleus when variant 1 starts to grow.

This coincides with Fig. 5a where the global elastic energy $E^{\text{el}} = \int_V W \, dV$ is plotted as a function of time for the simulations of Figs. 2 and 4. It can be seen that after the initial minimization, the elastic energy E^{el} starts to increase faster for two variants considered.

When the martensitic plate (i.e., the region where $c_1 = 1$) starts to grow within the austenitic matrix, due to the martensitic eigenstrain E^{el} increases. This results in the peak of E^{el} at $t = 80 \times 10^{-3} \text{ s}$ in Fig. 5a. The global elastic energy E^{el} diminishes when the plate has grown completely through the domain as the martensitic phase is now able to deform in a way that reduces E^{el} . In Fig. 4 at time step $t = 80 \times 10^{-3} \text{ s}$, a formation of the second variant has grown at the diagonally opposite edges of the matrix where the plate of the martensitic variant 1 ends. According to Yamanaka [21], the nucleation of variant 2 occurs in order to reduce

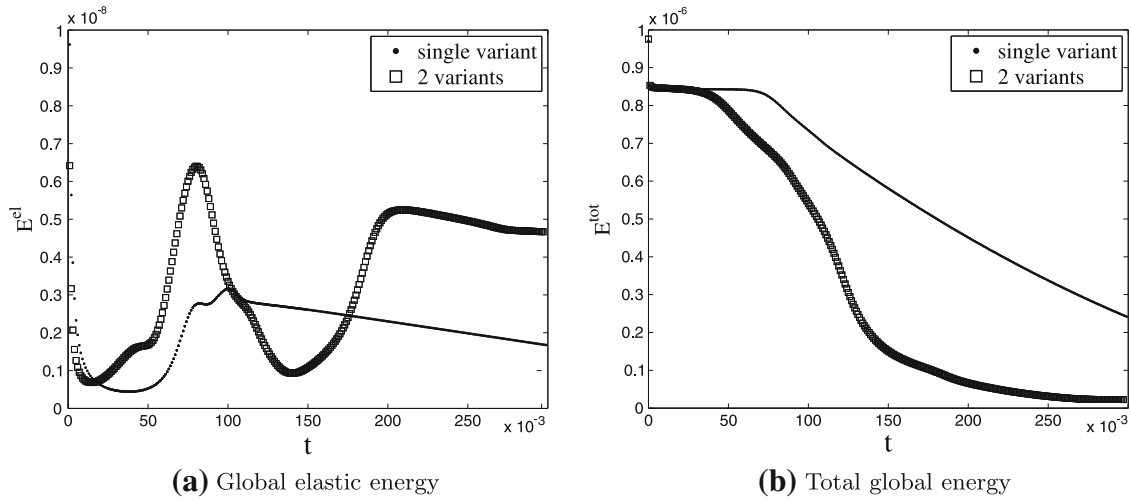


Fig. 5 Global energies plotted over the time for a single variant and two variants

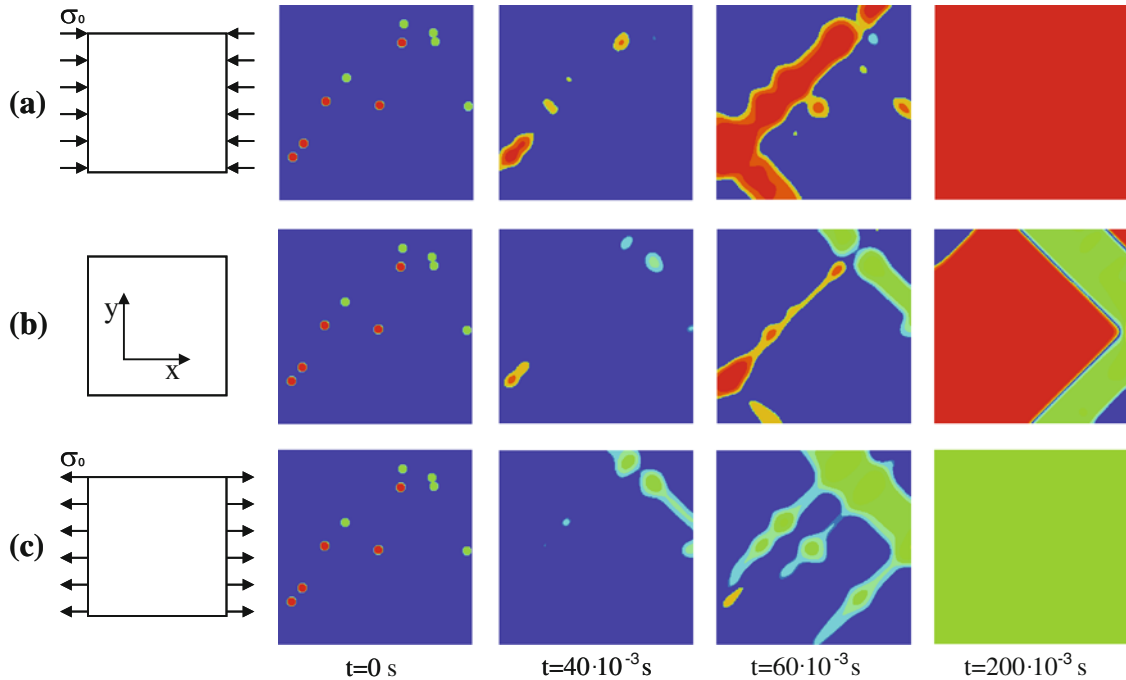


Fig. 6 Formation of the martensitic phase for randomly distributed circular nuclei for different load cases: **a** compression in x -direction, **b** no external load, **c** tension in x -direction

the transformation-induced stress. When the stress can be reduced by the deformation of the martensitic variant 1 plate at time step $t = 80 \times 10^{-3}$ s, the formation of variant 2 starts to retreat while the variant 1 plate extends at the lateral sides. Eventually, two variant 2 plates form at the two longer edges of the martensitic variant 1 phase (Fig. 4, $t = 200 \times 10^{-3}$ s) which leads to another local maximum of E^{el} (Fig. 5a). This corresponds to the results of Yamanaka [21], obtained with the finite difference method for the formation of martensitic microstructure in elastic materials, where variant 2 nucleates on the long edge of the variant 1 plate, too.

Figure 5b shows the total global energy $E^{tot} = \int_V \psi \, dV$ plotted as a function of time for the simulations in Fig. 2 and 4. It can be seen that E^{tot} decreases during both simulations. In comparison with two variants, however, for a single variant considered E^{tot} starts to decrease at a later time step caused by the delayed nucleation. Additionally, it decreases quite constantly whereas when considering two variants the curve changes slope in agreement with E^{el} . Furthermore, two variants reduce E^{tot} during 300 time steps by a higher amount because

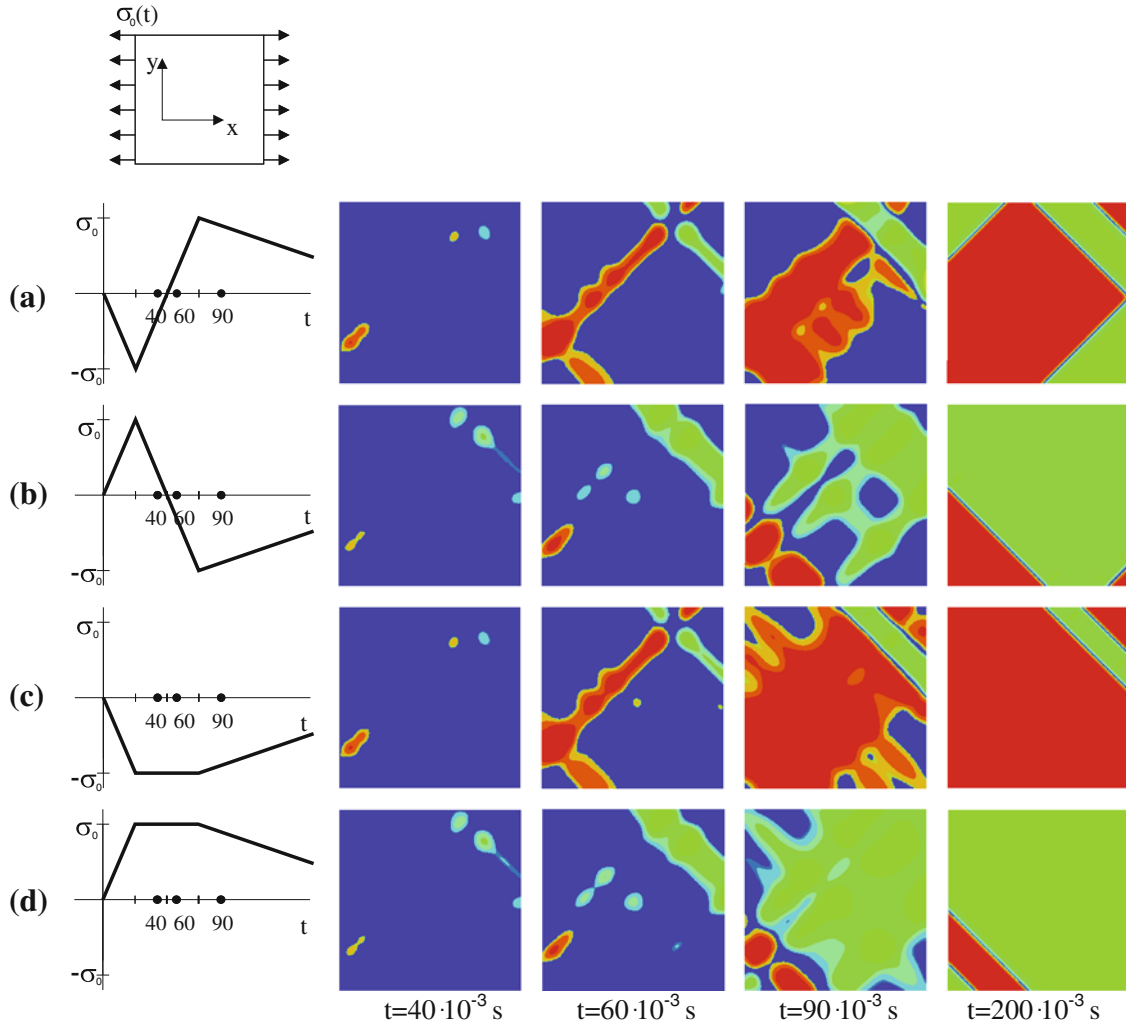


Fig. 7 Formation of the martensitic phase for randomly distributed circular nuclei with different load histories

more martensite is built than for a single variant, and the eigenstrains partly compensate on a macroscopic level.

4.4 Randomly distributed circular nuclei with external load

In the last section, the influence of an external load on the formation of the microstructure is studied. Therefore, five circular nuclei of each martensitic orientation are randomly distributed in the austenitic matrix. At first constant compression in x -direction is applied (Fig. 6a), then the example is calculated without external load (Fig. 6b), while for the third calculation constant tension in x -direction (same magnitude as for Fig. 6a) is considered (Fig. 6c). Obviously the load influences the martensitic formation. The transformation stress ϵ_1^0 correlates with pressure x -direction and tension in y -direction while ϵ_2^0 corresponds to tension in x -direction and pressure in y -direction. If pressure in x -direction is applied, variant 1 dominates, so that finally only this phase exists. Artemev et al. [1] attained the same result. For high stresses applied in one direction, the material contains finally only the corresponding variant. By analogy, tension in x -direction leads to a pure martensite variant 2 phase. For no external load at time step $t = 200 \times 10^{-3}$ s, both martensitic variants are formed while there is still some austenite present.

To examine the impact of load history on the evolution of the different phases, for the next simulations the load is varied linearly in time.

The structures shown in Fig. 7a result from the load histories which are depicted qualitatively on the left side. For Fig. 7a, a compression in x -direction is applied, followed by a tensile loading in x -direction, then the load is released. In analogy, for the second simulation (Fig. 7b), tension x -direction is followed by compression and load release. For the third and the fourth calculation, compression and tension are built up in x -direction, respectively. This load is held constant for 50 time steps and then released (Fig. 7c, d). It can be seen that the longer compression in x -direction is applied, the more martensitic variant 1 phase is formed. This is analogous for tension in x -direction and variant 2. However, for time step $t = 60 \times 10^{-3}$ s, the microstructures of Fig. 7a and Fig. 7c are very similar (as well as Fig. 7b and Fig. 7d) even though, after time step $t = 25 \times 10^{-3}$ s the two load histories are different. Thus, it takes some time for the system to react to changes in the load history. At time step $t = 90 \times 10^{-3}$ s, the differences between Fig. 7a and Fig. 7c (as well as Fig. 7b and Fig. 7d) are visible: For load case Fig. 7d, where only pressure in x -direction is applied, the fraction of martensite variant 1 is higher. So, the formation of the microstructure with its particular phases is influenced by the load history.

5 Summary

A phase field model for martensitic transformation is introduced with the time derivative of the order parameter assumed to follow the time-dependent Ginzburg–Landau equation. Simulations have shown that the martensitic phases form in accordance with theoretical studies and crystallographic theories while the nucleation behavior of the model is adaptable. A basic understanding of the energy evolution during the formation of martensitic phases could be gained where two variants minimize the total energy more effective than a single variant. Additionally, a relation between the direction of a time-dependent external loading and the evolution of different martensitic orientations could be worked out.

For future work, we plan to combine information gained from atomistic simulation with continuum modeling to study the transformation dynamics on different time and space scales.

Acknowledgments This work was financially supported by the Deutsche Forschungsgemeinschaft, SFB 926.

References

1. Artemev, A., Wang, Y., Khachaturyan, A.G.: Three-dimensional phase field model and simulation of martensitic transformation in multilayer systems under applied stresses. *Acta. Mater.* **48**, 2503–2518 (2000)
2. Bartel, T., Menzel, A., Svendsen, B.: Thermodynamic and relaxation based modeling of the interaction between martensitic phase transformations and plasticity. *J. Mech. Phys. Solids* **59**, 1004–1019 (2011)
3. Chen, L.Q., Wang, Y., Khachaturyan, A.G.: Kinetics of twinned and twin formation during an ordering transition in a substitutional solid solution. *Philos. Mag. Lett.* **65**(1), 15–23 (1992)
4. Cherkaoui, M., Berveiller, M.: Micromechanical modeling of the martensitic transformation induced plasticity steels. *Smart Mater. Struct.* **9**, 592–603 (2000)
5. Engin, C., Urbassek, H.M.: Molecular dynamics investigation of the fcc \rightarrow bcc phase transformation in Fe. *Comput. Mater. Sci.* **41**, 297–304 (2008)
6. Entel, P., Meyer, R., Kadau, K.: Molecular dynamics simulations of martensitic transformations. *Phil. Mag. B.* **80**, 183–194 (2000)
7. Fischer, F.D., Berveiller, M., Tanaka, K., Oberaigner, E.R.: Continuum mechanical aspects of phase transformations in solids. *Arch. Appl. Mech.* **64**, 54–85 (1994)
8. Gao, L.F., Feng, X.Q., Gao, H.: A phase field method for simulating morphological evolution of vesicles in electric fields. *J. Comput. Phys.* **228**, 4162–4181 (2009)
9. Hildebrand, F., Miehe, C.: A regularized sharp interface model for phase transformation accounting for prescribed sharp interface kinetics. *Proc. Appl. Math. Mech.* **10**, 673–676 (2010)
10. Hildebrand, F.E., Miehe, C.: Comparison of two bulk energy approaches for the phasefield modeling of two-variant martensitic laminate microstructure. *Techn. Mech.* **32**, 3–20 (2012)
11. Jin, Y.M., Artemev, A., Khachaturyan, A.G.: Three dimensional phase field model of low-symmetry martensitic transformation in polycrystal: Simulations of ζ_2' martensite in AuCd alloys. *Acta. Mater.* **49**, 2309–2320 (2001)
12. Kundin, J., Raabe, D., Emmerich, H.: A phase-field model for incoherent martensitic transformations including plastic accommodation processes in the austenite. *J. Mech. Phys. Solids* **59**, 2082–2102 (2011)
13. Levitas V.I., Lee D.-W., Preston D.L.: Interface propagation and microstructure evolution in phase field models of stress-induced martensitic phase transformations. *Int. J. Plast.* (2009) doi:[10.1016/j.ijplas.2009.08.003](https://doi.org/10.1016/j.ijplas.2009.08.003)
14. Rubini, S., Ballone, P.: Quasiharmonic and molecular-dynamics study of the martensitic transformation in Ni-Al alloys. *Phys. Rev. B* **48**, 99–111 (1993)
15. Sandoval, L., Urbassek, H.M.: Transformation pathways in the solid-solid phase transitions of iron nanowires. *Appl. Phys. Lett.* **95**, 191909 (2009)

16. Schrader, D., Mueller, R., Xu, B.X., Gross, D.: Domain evolution in ferroelectric materials: a continuum phase field model and finite element implementation. *Comput. Methods Appl. Mech. Eng.* **196**, 4365–4374 (2007)
17. Schrader, D., Xu, B.X., Müller, R., Gross, D.: On phase field modeling of ferroelectrics: parameter identification and verification. *SMASIS* **2008**(1), 299–306 (2008)
18. Schrader, D., Müller, R., Gross, D.: Parameter identification in phase field models for ferroelectrics. *Proc. Appl. Math. Mech.* **9**, 369–370 (2009)
19. Wang, Y., Khachaturyan, A.G.: Three-dimensional field model and computer modeling of martensitic transformations. *Acta. Mater.* **45**(2), 759–773 (1997)
20. Wechsler, M.S., Lieberman, D.S., Read, T.: On the theory of the formation of martensite. *Trans. AIME* **197**, 1503–1515 (1953)
21. Yamanaka, A., Takaki, T., Tomita, Y.: Elastoplastic phase-field simulation of self- and plastic accommodations in cubic \rightarrow tetragonal martensitic transformation. *Mater. Sci. Eng. A.* **491**, 378–384 (2008)
22. Zhang, W., Jin, Y.M., Khachaturyan, A.G.: Phase field microelasticity modeling of heterogeneous nucleation and growth in martensitic alloys. *Acta. Mater.* **55**, 565–574 (2007)